

pubs.acs.org/acsaelm Article

Bias Dependence of Organic-Oxide Phototransistors with Peak Infrared Absorption at 1550 nm

Bogyeom Seo, Jusung Chung, Naresh Eedugurala, Jason D. Azoulay, Hyun Jae Kim, and Tse Nga Ng*



Cite This: https://doi.org/10.1021/acsaelm.3c01276



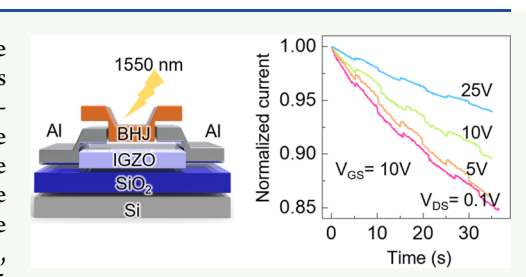
ACCESS I

III Metrics & More

Article Recommendations

SI Supporting Information

ABSTRACT: Photodetectors operating across the short-wave infrared region are essential elements of modern optoelectronic technologies. This work demonstrates the integration of an organic bulk heterojunction polymer layer on an oxide thin-film transistor to achieve a peak infrared photoresponse at 1550 nm. As the efficiency of organic semiconductors decreases at longer wavelengths, the phototransistor structure uses trap-assisted charge injection to enhance the photoresponse. This work optimizes the detector performance by investigating the balance between bias stress and signal-to-noise under different bias conditions, enabling a responsivity at 1550 nm up to 130 mA/W at a low light intensity of 2.5 \times 10^{-5} W/cm².



KEYWORDS: infrared polymer, organic bulk heterojunction, indium gallium zinc oxide, phototransistor, bias stress

INTRODUCTION

Infrared detectors are essential to modern optoelectronic technologies, such as spectroscopy and machine vision applications. However, for devices operating in the shortwave infrared (SWIR, wavelength $\lambda = \sim 1$ to 1.7 μ m), conventional and costly epitaxial semiconductors are the dominant technology. There are ongoing efforts to develop alternative semiconductors that facilitate low-cost, monolithic detector fabrication. Among these emerging technologies, organic semiconductors such as donor—acceptor conjugated polymers 12 enable facile and scalable processing and functionality to infrared wavelengths beyond 1 μ m. However, according to the energy-gap law, as the bandgap of organic semiconductors decreases, the recombination rate of photogenerated excitons increases, leading to a decline in device efficiency at longer wavelengths.

To improve the photoresponse of organic infrared detectors, researchers have used the mechanism of trap-assisted charge injection which amplifies the photocurrent. Here, we leverage such external charge injection to increase the signal from an organic bulk heterojunction (BHJ) film with a peak absorption at 1550 nm, which is notably far into the infrared in comparison with the majority of organic photodetectors today. We integrate the infrared-responsive BHJ into wide bandgap indium gallium zinc oxide (IGZO) thin-film transistors (TFT), 19,20 which exhibit very low off-current and are insensitive to infrared radiation for suppressing background noise. In contrast to two-terminal photodiodes, the architecture of three-terminal photo thin-film transistors (photoTFT) 19-22 separates the processes of charge photogeneration and transport within the BHJ and IGZO, respectively. This simplifies the optimization of each layer.

In analyzing the operation of the infrared photoTFTs, this paper considers the bias stress effect^{23–28} inherent in transistors using disordered semiconductors like IGZO. The bias stress effect occurs because of the trapping of mobile carriers, resulting in a gradual decrease in source-drain current over time. This work presents the trade-offs between bias stress, photocurrent, and dark current noise as functions of the applied biases, in order to select appropriate biases that optimize the device performance. The rationale here can be generalized to other photoTFTs beyond those based on organics and IGZO. After the optimal bias conditions are identified, the detectivity, response time, and responsivity of the photoTFTs are determined as a function of incident light intensity.

■ RESULTS AND DISCUSSION

The chemical structures and energy levels of the narrow-bandgap organic semiconductors are shown in Figure 1(a,b), respectively. The donor polymer poly(4-(5-(4-(3,5-bis-(dodecyloxy)benzylidene)-4H-cyclopenta[2,1-b:3,4-b']-dithiophen-2-yl)thiophen-2-yl)-6,7-dioctyl-9-(thiophen-2-yl)[1,2,5]thiadiazolo[3,4-g]quinoxaline) has a highest occupied molecular orbital (HOMO) energy level of -4.7 eV and the lowest unoccupied molecular orbital (LUMO) energy level of -3.8 eV, corresponding to an absorption maximum (λ_{max}) of

Received: September 13, 2023 Revised: October 27, 2023 Accepted: October 30, 2023



ACS Applied Electronic Materials

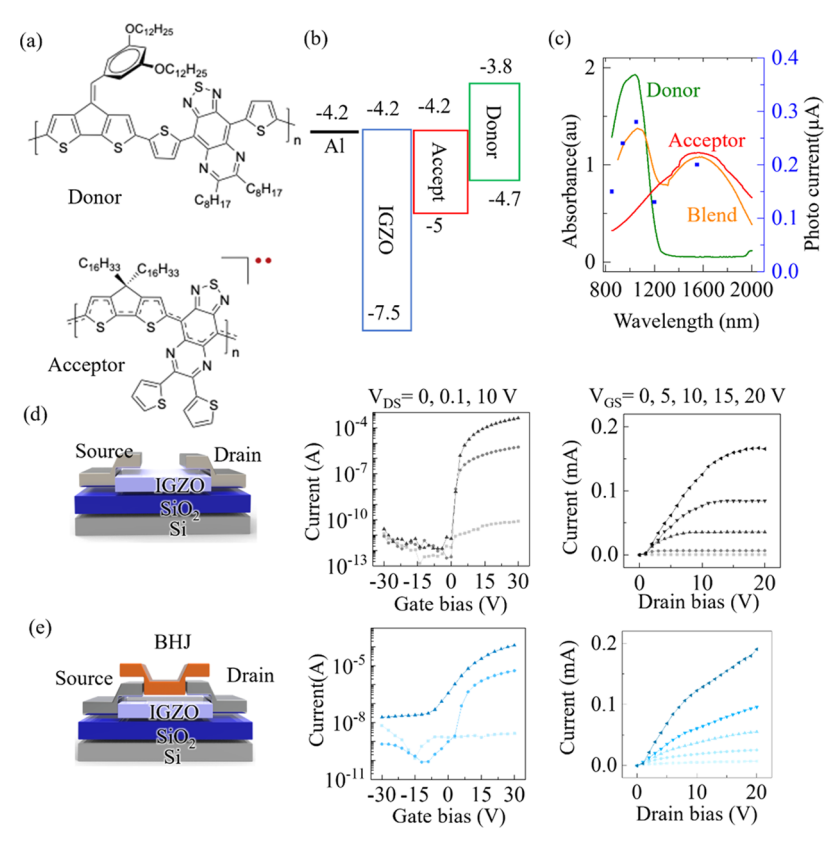


Figure 1. (a) Chemical structures of the two conjugated polymers used in the BHJ film. (b) Energy levels of materials used in the device. (c) Absorption spectra of the donor, acceptor, 1:2 donor:acceptor blend, and photoTFT response (blue symbols) at different wavelengths. Schematics and transistor characteristics of (d) IGZO and (e) IGZO with BHJ; measurements were taken in the dark.

1100 nm [Figure 1(c)].²⁹ The acceptor polymer poly (4-(4,4dihexadecyl-4*H*-cyclopenta[2,1-*b*:3,4-*b*']dithiophen-2-yl)-6,7di(thiophen-2-yl)-[1,2,5]thiadiazolo[3,4-g]quinoxaline)has a HOMO energy level of -5 eV and the LUMO energy level of -4.2 eV, corresponding to $\lambda_{\text{max}} = 1550$ nm in the SWIR.³⁰ The absorption throughout the SWIR is related to extensive π conjugation, which also leads to an open-shell electronic structure. The open-shell electronic structure arises from a high degree of electronic coherence along the conjugated backbone. The donor and acceptor units promoted strong π electron correlations and extensive delocalization to enable a very narrow bandgap. This enables strong configuration mixing between the frontier molecular orbitals (i.e., HOMO and LUMO mixing) stabilizing unpaired spins in the backbone.³¹ The BHJ film comprised a blend of the donor and acceptor at a 1:2 ratio, with the absorption characteristics shown in Figure 1(c). Other donor-acceptor ratios were explored and are shown in Supplemental Figure S1. We also tried to use a film consisting of only the acceptor, but the photoresponse was very weak (Supplemental Figure S2). The BHJ film with higher interfacial areas facilitated more charge dissociation than a film with only the acceptor, and therefore we selected the BHJ configuration.

The device structure and current—voltage characteristics of a thin-film transistor (TFT) with an IGZO semiconductor are shown in Figure 1(d). The threshold voltage ($V_{\rm th}$) was 0 V, and the effective charge mobility inside the IGZO channel was determined to be up to 13.3 cm²/(V s) in the saturation region, ³⁰ which was within the typical range for IGZO TFTs. IGZO alone was not sensitive to infrared light due to its wide bandgap of ~3.3 eV (HOMO: -7.5 eV; LUMO: -4.2 eV).

Thus, to realize a photoTFT that would be responsive to infrared light, the organic BHJ blend was patterned on top of the IGZO channel, as depicted in Figure 1(e).

The BHJ facilitated the absorption of infrared photons and the subsequent generation of excitons to be transduced into an electrical current. However, within the present configuration, the BHJ layer contributed an additional bulk conduction path between the source and drain electrodes. This effect was evident in the transfer characteristics as an increase in the offcurrent and shallow subthreshold slopes and in the output characteristics a lack of current saturation. While reducing the BHJ layer thickness decreased the TFT off-current, this occurred at the expense of poor light absorption (Supplemental Figure S3); thus, a BHJ layer thickness of 160 nm was utilized. In the future, the BHJ area may be adjusted to avoid bridging the source and drain electrodes or an insulating material may be deposited on top of the electrodes to block conduction via the BHJ. While more can be done to refine the device in Figure 1(e), it was sufficient for our goal to study the impact of bias conditions on balancing detectivity and bias stress in infrared photoTFTs. Thus, we proceeded to examine the photoresponse by systematically varying the drain bias while holding the gate bias at a fixed voltage, or vice versa, to determine guidelines for enhancing photoTFT performance through operating at optimal biases.

The star markers in Figure 2(a) indicate the experimental parameters of varying the drain bias $(V_{\rm DS})$ as the applied gate bias $(V_{\rm GS})$ was set at the same voltage of 10 V. In Figure 2(b), the source-drain current was measured over time, and the current was normalized to the initial value at time t=0 s. This measurement was carried out to evaluate the bias stress

ACS Applied Electronic Materials

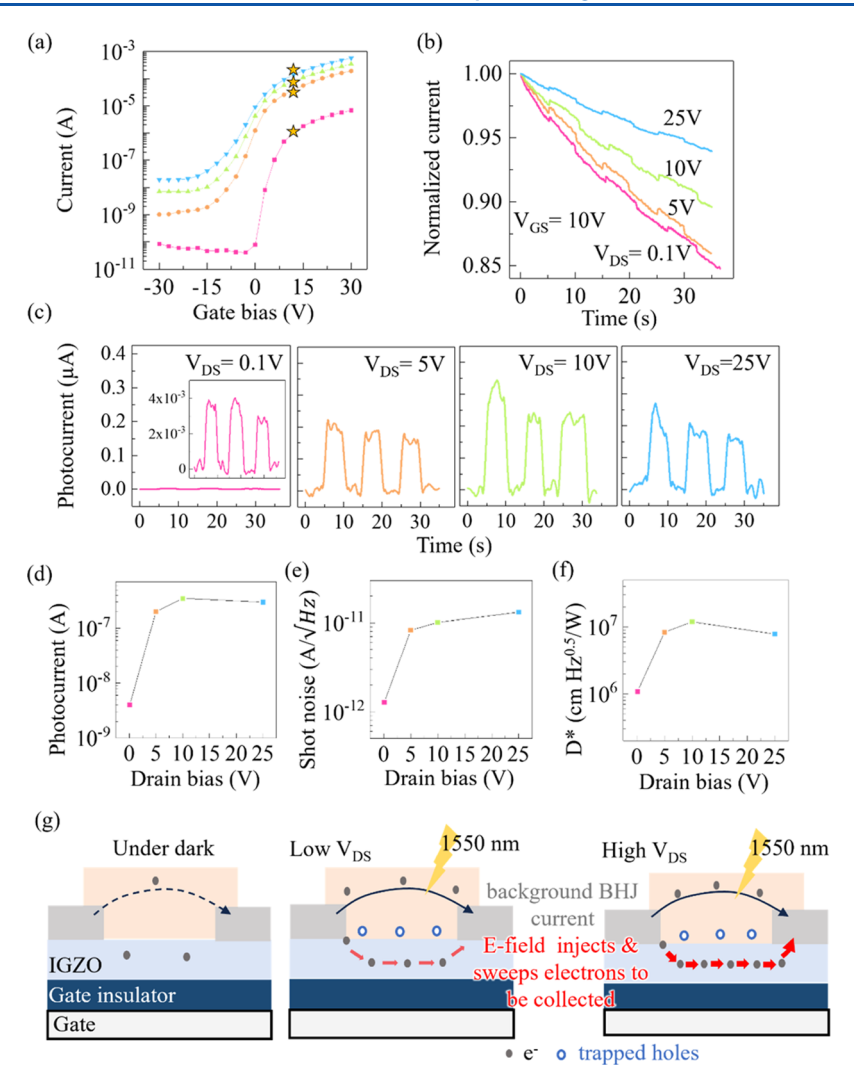


Figure 2. Comparison of device characteristics when operating with a fixed gate bias of $V_{\rm GS}=10$ V while $V_{\rm DS}$ is varied. (a) Transfer characteristics of a typical BHJ-IGZO transistor in the dark. The star markers denote the bias conditions for the subplots. (b) Normalized source-drain current as a function of time. All photoresponse data in this figure were taken under incident light pulses from a 1550 nm laser diode at a power of 15 mW/cm². (c) Photocurrent after background subtraction, which removed the drift due to bias stress. (d) Photocurrent, (e) calculated shot noise, and (f) detectivity of the photoTFT as a function of $V_{\rm DS}$. (g) Illustration comparing the device currents in the dark and under illumination upon applying a low or high bias between the source-drain electrodes.

phenomena, 24,27 which was a gradual drop in transistor sourcedrain current due to charge trapping inherent in noncrystalline semiconductors and typically mitigated by operating the device under duty cycles, so trapped charges could be released and the device would reach a stable operating condition. The normalized comparison shows that when the applied $V_{\rm DS}$ increased, the rate of current decay decreased. Namely, the bias stress degradation was mitigated as the device approached its saturation region of $V_{\rm DS} \geq V_{\rm GS} - V_{\rm th}$. This improvement in the current stability was attributed to the increased ratio of injected charges to trapped charges. Under a fixed gate bias, the amount of trapped charges remained relatively constant in the TFT channel. Meanwhile, the higher lateral electric field with rising $V_{\rm DS}$ would inject more mobile electrons from the Al electrodes into the channel; consequently, the drop in normalized current was less severe at higher $V_{\rm DS}$ because the proportion of trapped charges became smaller in relation to mobile electrons.

In Figure 2(b), the device was subjected to light modulation, switching every 5 s between being in the dark to being

illuminated under 1550 nm light at 15 mW/cm² from a laser diode. The measurements clearly display the step changes resulting from photocurrent generation under the 5 s light pulses. The current drift due to bias stress was subtracted from the data to yield Figure 2(c), which compares the photocurrent magnitudes obtained at different $V_{\rm DS}$'s while $V_{\rm GS}=10$ V. The photocurrent was 4 nA at $V_{\rm DS}=0.1$ V and increased by nearly 60-fold to 250 nA at $V_{\rm DS}=25$ V. This dependence of photocurrent on $V_{\rm DS}$ is summarized in Figure 2(d).

Then, in addition to the signal magnitudes, the background noise levels are also an important consideration for photodetectors to improve the detection limit (i.e., detectivity). The dark current noise as a function of $V_{\rm DS}$ is presented in Figure 2(e). The measured noise values^{32–34} (Supplemental Figure S3) were obtained via a lock-in amplifier, and the values are 5-fold higher than the calculated shot noises from the equation $\sqrt{2qI_{\rm dark}} \ \Delta f$ in Figure 2(e), where q is the electron charge, $I_{\rm dark}$ is the dark current, and Δf is the detection bandwidth, which is 8 Hz here. The dark current noise increased from 3.5 pA/Hz^{0.5} at $V_{\rm DS}$ = 0.1 V to 19 pA/Hz^{0.5} at $V_{\rm DS}$ = 25 V. We computed the

detectivity (D^*) in Figure 2(f) with an adjustment ratio of 0.2 (=1/5), to compensate for the difference between measured noise and calculated shot noise (5-fold higher value for the measured noise than the calculated shot noise), so as to not underestimate the noise in D^* calculations. Because the photocurrent and the background noise both increased with $V_{\rm DS}$, the photoTFT D^* reached a plateau of 10^7 cmHz^{0.5}/W around $V_{\rm DS}$ = 10 V, at the light intensity of 15 mW/cm².

The operation of the photoTFT is illustrated in Figure 2(g), which contrasts the effect of applied $V_{\rm DS}$ at low or high voltage. When infrared light generated excitonic electron-hole pairs in the BHJ, it would be energetically favorable for the electrons to be collected at the electrodes or transferred to the n-type IGZO layer, leaving behind holes in the BHJ. The trapped holes in the BHJ effectively acted as an additional back-gate bias for the TFT channel to promote more electron accumulation in the IGZO. When the lateral electric field increased between the source and drain electrodes, more electrons would be injected and collected across the IGZO channel, resulting in the rise of photocurrent with higher $V_{\rm DS}$. On the other hand, a high $V_{\rm DS}$ also led to more background charge flow in the BHJ layer and raised the dark current noise. Overall, at a fixed V_{GS} , increasing the V_{DS} would lower bias stress and enhance photocurrent. However, the concurrent increase in noise would eventually affect the photoTFT detectivity causing it to reach a plateau. Next, we examined the converse conditions where V_{DS} is fixed while V_{GS} was

As indicated by the corresponding markers in Figure 3(a), the bias conditions for the bias stress measurements in Figure 3(b) were at constant $V_{\rm DS}=10~\rm V$ as the gate bias $V_{\rm GS}$ changed from 0 to 20 V. Higher $V_{\rm GS}$ would place the photoTFT more toward operating in the linear region ($V_{\rm DS} < V_{\rm GS} - V_{\rm th}$), and the device showed a more severe decay of the normalized current as $V_{\rm GS}$ increased. This is in agreement with the trend in Figure 2(b), where it is observed that operation in the saturation region was more favorable for reducing bias stress because more of the channel carriers were collected by the high lateral electric field between the source and drain electrodes.

The bias stress drift was subtracted from Figure 3(b) to present the photocurrent clearly in Figure 3(c), which was taken under light pulses of 15 mW/cm² from a 1550 nm laser diode. For $V_{\rm GS}$ = 0 V, the bias stress drift was the lowest, but the photocurrent was also very low at around 4 nA only. The photocurrent was approximately 20 nA at V_{GS} = 5 V, 300 nA at $V_{\rm GS}$ = 10 V, and 350 nA at $V_{\rm GS}$ = 20 V. The rise in photocurrent leveled off and the dark current noise rose with increasing V_{GS} as seen in Figure 3(d,e), respectively. As the source-drain bias $V_{\rm DS}$ was held constant while the gate bias $V_{\rm GS}$ was varied, the photocurrent increased. This response suggested that increasing V_{GS} helped to transfer charge across the BHJ-IGZO barrier, resulting in higher photocurrent. This effect might also come from increasing the mobility with higher V_{GS} , contributing to the photocurrent increase. Both mobility and charge transfer were contributing factors to increase the charge collection 35 and photocurrent with V $_{GS}$. In Figure 3(f), the detectivity as a function of V_{GS} shows a

In Figure 3(f), the detectivity as a function of $V_{\rm GS}$ shows a peak value of 1.2×10^7 cmHz^{0.5}/W with $V_{\rm GS} = 10$ V and $V_{\rm DS} = 10$ V. This D^* value is calculated by including the ratio between the measured noise and the shot noise, similar to Figure 2(f). The schematics of Figure 3(g) show the effect of increasing the gate bias to facilitate charge transfer from BHJ to the IGZO channel. However, the higher number of

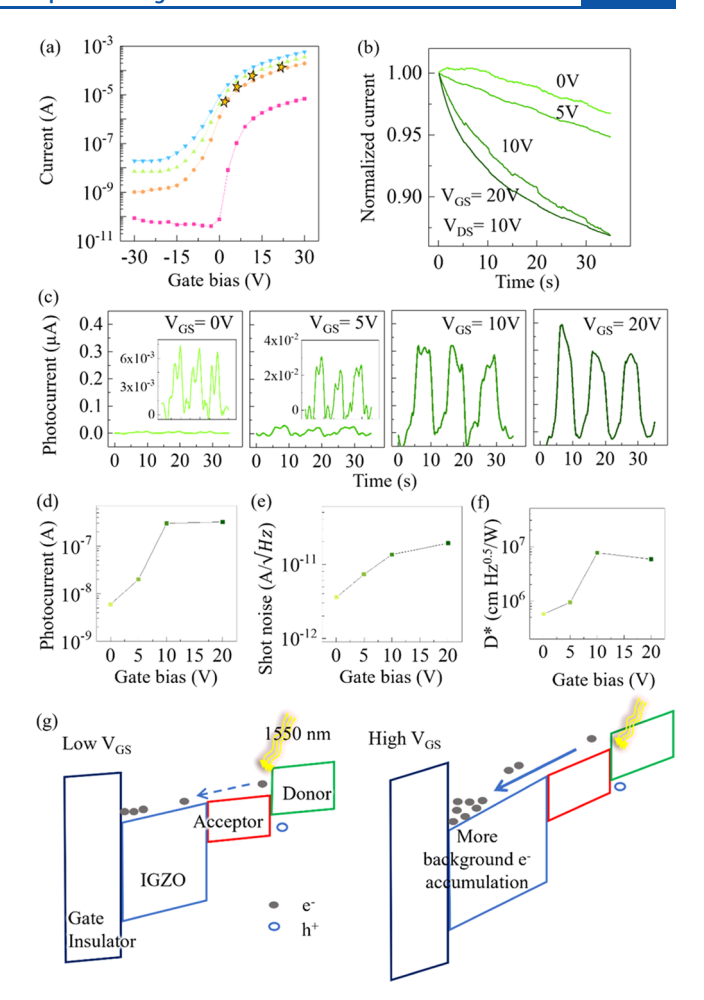


Figure 3. Comparison of device characteristics when operating with a fixed source-drain bias $V_{\rm DS}=10$ V while $V_{\rm GS}$ is varied. (a) Transfer characteristics of a typical BHJ-IGZO transistor in the dark. The star markers denote the bias conditions for the subplots. (b) Normalized source-drain current as a function of time. All photoresponse data in this figure were taken under incident light pulses from a 1550 nm laser diode at 15 mW/cm². (c) Photocurrent after background subtraction, which removed the drift due to bias stress. (d) Photocurrent, (e) calculated shot noise, and (f) detectivity of the photoTFT as a function of $V_{\rm GS}$. (g) Illustration comparing the charge transfer between BHJ and IGZO layers to generate trapped holes, upon applying a low or high gate bias.

accumulated electrons in the IGZO channel with increasing $V_{\rm GS}$ would increase the background noise current.

As a generalization, the optimal bias conditions for the photoTFT are found to be at the verge of the transition between linear and saturation regions to balance the target characteristics of bias stress, photocurrent, and noise. The bias stress effect and photocurrent are improved by operating in the saturation region; yet if the applied biases are further increased, the rise in dark current noise offsets the photocurrent increase. Thus, it would be most effective to choose selecting applied biases that place the photoTFT at the transition boundary of $V_{\rm DS} \sim V_{\rm GS} - V_{\rm th}$, on account of the competing trends among the performance metrics to maximize device detectivity and stability.

With the insights from Figures 2 and 3, the photoTFT was set to operate at an optimal bias of $V_{\rm GS} = V_{\rm DS} = 10~{\rm V}$ in Figure 4. The device performance was further characterized on its dependence on the incident light intensity and pulse

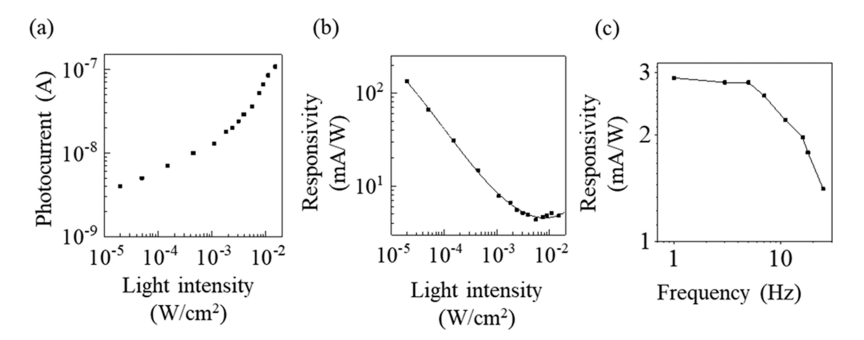


Figure 4. PhotoTFT biased at $V_{GS} = V_{DS} = 10 \text{ V}$ and measured under incident light pulses from a 1550 nm laser diode. (a) Photocurrent and (b) responsivity as a function of light intensity, under light pulses switching at 1 Hz. (c) Responsivity as a function of light modulation frequency, with the light intensity set at 9 mW/cm².

frequency. The photocurrent as a function of light intensity is shown in Figure 4(a), with a distinguishable photoresponse indicating a noise equivalent power (NEP) of 2.5×10^{-5} W/cm², where NEP is related to detectivity by NEP = $(A\Delta f)^{0.5}/D^*$. With the detector area A of 1.5×10^{-3} cm², the measured NEP level was equivalent to a detectivity of 7×10^6 cmHz^{0.5}/W, in agreement with the values reported in Figures 2(f) and 3(f).

The photocurrent in Figure 4(a) was converted to responsivity (R = photocurrent/incident light power) in Figure 4(b), which indicated an increasing responsivity with a lower incident light intensity. This characteristic had been observed and explained in other photoTFT works which, similar to our device here, leveraged trap-assisted charge injection to boost the photocurrent. The photocurrent is proportional to the ratio of trap lifetime to charge transit time $(\tau_{\text{trap}}/\tau_{\text{transit}})$. At low light intensities, the trap lifetime was longer due to a lower probability of recombination than at high light intensities, and therefore, charge injection was increased and raised the responsivity. This feature was helpful in enhancing the photoresponse to weak light levels. At the low light intensity of 10^{-5} W/cm², the responsivity is shown to be 130 mA/W, and converting that to external quantum efficiency (EQE), it is equivalent to an EQE of 8% at 1550 nm.

Lastly, the photoTFT response speed is shown in Figure 4(c), where the -3 dB cutoff frequency was around 10 Hz. The response speed of this photoTFT was slow due to the time needed for charge injection and transport across the TFT channel, but, as a future direction, the operation could be readily improved by reducing the channel length to shorten the charge transit time for a faster response.

CONCLUSIONS

This paper presents an infrared detector combining BHJ polymers with IGZO TFT structures to achieve a peak response to 1550 nm light. The response to this infrared wavelength was enabled by the BHJ photogeneration and subsequent trap-assisted charge injection in the IGZO TFT. The performance of the photoTFT was examined with respect to different gate and drain biases, and it was shown that operation around the transition between linear and saturation regions offered an optimal bias condition that would maximize the device signal-to-noise ratio and stability. The photoTFT achieved a responsivity of 130 mA/W, equivalent to an EQE of 8%, under a low light intensity of 2.5×10^{-5} W/cm² and a detectivity of 7×10^6 cmHz^{0.5}/W with the $V_{\rm GS} = V_{\rm DS} = 10$ V. These findings provide feasibility demonstration of photoTFTs

responsive to the 1550 nm spectral range and suggest pathways to improve these infrared devices based on low-cost, scalable organic and oxide semiconductors.

EXPERIMENTAL METHODS

Materials and Device Fabrication. The donor and acceptor polymers used in this study are synthesized by microwave-assisted reactions, as detailed in refs 29,30,37,38, respectively. The IGZO TFTs were prepared on a p-type Si substrate with 120 nm of SiO₂ on the surface serving as the gate dielectric with a capacitance of 28.8 nF/ cm². The IGZO channel was deposited by sputtering to form a 50 nm thickness of film. The source and drain electrodes were deposited by thermal evaporation of aluminum and patterned to form a TFT channel of width $W=1000~\mu m$ and length of $L=150~\mu m$. After the IGZO TFTs were completed, the BHJ layer was spin-coated on top of the IGZO to form a film with a thickness of 160 nm. The solution of the BHJ was a mixture of the donor and acceptor polymers at a weight ratio of 1:2, dissolved in dichlorobenzene at a total concentration of 27 mg/mL. The solution was heated to 90 °C and stirred overnight to ensure dissolution of the polymers. The BHJ film was patterned by wiping away materials with cotton swaps soaked in dichlorobenzene, and the BHJ area was 2 mm × 1 mm over each IGZO TFT. The devices were placed in vacuum for 10 min to remove residual solvent. The BHJ processing was carried out within a nitrogen glovebox, and the devices were measured in the ambient environment without encapsulation.

Device Characterization. During measurements, the source and drain terminals of the photoTFTs were connected to a picoammeter (Keithley 6485), and the gate terminal was connected to another electrometer (Keithley 2400), and both meters shared a common ground, with the source electrode of the TFT connected to ground. The infrared light source was a 1550 nm laser diode (Thorlabs, part number ML925B45F). The light intensity was controlled by adjusting the applied bias to the laser diode, and a function generator (Rigol, DG 2401A) was used to modulate the light pulse frequency. A germanium detector from Newport (model: 818IR) was the reference light meter for the calibration of the light source.

After measurement of the current—voltage characteristics, the TFT transfer characteristics in the dark were fitted to the gradual channel approximation model for extraction of the effective charge mobility. The model equation was $\mu = \frac{L\partial l_{\rm DS}}{WCV_{\rm DS}\partial V_{\rm GS}}$, where μ is the mobility, L is the channel length, W is the channel width, and C is the oxide capacitance.

To measure the noise spectral density, a preamplifier (Stanford Research Systems model 570) was connected to a lock-in amplifier (Stanford Research Systems model 530). The reference frequency for the noise measurements was controlled by a function generator (Rigol, DG 2401A), which acted as the external trigger for the lock-in amplifier. To obtain the device noise, the background noise of the equipment was subtracted from the measurements. The detectivity was calculated from the relation $D^* = \frac{R\sqrt{A}}{r}$, where R is the

responsivity, A is the channel area, and I_n is the calculated noise. The external quantum efficiency was calculated from EQE = $(R/\lambda)(hc/q)$, where λ is the wavelength, h is Planck's constant, and c is the speed of light.

ASSOCIATED CONTENT

Solution Supporting Information

The Supporting Information is available free of charge at https://pubs.acs.org/doi/10.1021/acsaelm.3c01276.

The Supporting Information is available on the journal Web site. Device characteristics of photoTFTs with different donor:acceptor ratios (Figure S1); photoresponse of a photoTFT in which the absorption layer consisted of only the acceptor polymer instead of a BHJ (Figure S2); photocurrent of devices with different BHJ film thicknesses (Figure S3); measurements of noise spectral density (Figure S4); and spectral response of the photoTFT (Figure S5) (PDF)

AUTHOR INFORMATION

Corresponding Author

Tse Nga Ng — Department of Electrical and Computer Engineering, University of California San Diego, La Jolla, California 92093-0407, United States; orcid.org/0000-0001-6967-559X; Email: tnn046@ucsd.edu

Authors

- Bogyeom Seo Department of Electrical and Computer Engineering, University of California San Diego, La Jolla, California 92093-0407, United States
- Jusung Chung Department of Electrical and Electronic Engineering, Yonsei University, Seoul 03722, Republic of Korea
- Naresh Eedugurala School of Chemistry and Biochemistry and School of Materials Science and Engineering, Georgia Institute of Technology, Atlanta, Georgia 30332, United States
- Jason D. Azoulay School of Chemistry and Biochemistry and School of Materials Science and Engineering, Georgia Institute of Technology, Atlanta, Georgia 30332, United States;
 orcid.org/0000-0003-0138-5961
- Hyun Jae Kim Department of Electrical and Electronic Engineering, Yonsei University, Seoul 03722, Republic of Korea; ⊚ orcid.org/0000-0002-6879-9256

Complete contact information is available at: https://pubs.acs.org/10.1021/acsaelm.3c01276

Notes

The authors declare no competing financial interest.

ACKNOWLEDGMENTS

B.S. and T.N.N. are supported by the National Science Foundation (NSF) award ECCS-2222203. The work performed at The Georgia Institute of Technology was made possible through the Air Force Office of Scientific Research (AFOSR) under the support provided by the Organic Materials Chemistry Program (Grant FA9550-23-1-0654, Program Manager: Dr. Kenneth Caster) and the NSF award DMR-2323665.

REFERENCES

- (1) Rogalski, A. Infrared and Terahertz Detectors, 3rd ed.; CRC Press, 2019.
- (2) Rogalski, A.; Kopytko, M.; Martyniuk, P. Two-Dimensional Infrared and Terahertz Detectors: Outlook and Status. *Appl. Phys. Rev.* **2019**, *6* (2), 021316 DOI: 10.1063/1.5088578.
- (3) García de Arquer, F. P.; Armin, A.; Meredith, P.; Sargent, E. H. Solution-Processed Semiconductors for next-Generation Photodetectors. *Nat. Rev. Mater.* **2017**, *2* (3), 16100.
- (4) Li, N.; Mahalingam, P.; Vella, J. H.; Leem, D.-S. S.; Azoulay, J. D.; Ng, T. N. Solution-Processable Infrared Photodetectors: Materials, Device Physics, and Applications. *Mater. Sci. Eng. R-Rep.* **2021**, *146* (August), No. 100643.
- (5) Wang, C.; Zhang, X.; Hu, W. Organic Photodiodes and Phototransistors toward Infrared Detection: Materials, Devices, and Applications. *Chem. Soc. Rev.* **2020**, 49, 653–670.
- (6) Jacoutot, P.; Scaccabarozzi, A. D.; Nodari, D.; Panidi, J.; Qiao, Z.; Schiza, A.; Nega, A. D.; Dimitrakopoulou-Strauss, A.; Gregoriou, V. G.; Heeney, M.; Chochos, C. L.; Bakulin, A. A.; Gasparini, N. Enhanced Sub-1 EV Detection in Organic Photodetectors through Tuning Polymer Energetics and Microstructure. *Sci. Adv.* **2023**, *9*, No. eadh2694.
- (7) Li, N.; Eedugurala, N.; Leem, D. S.; Azoulay, J. D.; Ng, T. N. Organic Upconversion Imager with Dual Electronic and Optical Readouts for Shortwave Infrared Light Detection. *Adv. Funct Mater.* **2021**, *31*, No. 2100565.
- (8) Yu, X.; Lin, H.; He, Z.; Du, X.; Chen, Z.; Yang, G.; Zheng, C.; Tao, S. Efficient Near-Infrared Organic Photodetectors with Spectral Response up to 1600 Nm for Accurate Alcohol Concentration Detection. ACS Appl. Mater. Interfaces 2023, 15 (13), 16918–16929. (9) Li, T.; Hu, G.; Tao, L.; Jiang, J.; Xin, J.; Li, Y.; Ma, W.; Shen, L.; Fang, Y.; Lin, Y. Sensitive Photodetection below Silicon Bandgap Using Quinoid-Capped Organic Semiconductors. Sci. Adv. 2023, 9, No. eadf6152.
- (10) Han, J.; Yang, D.; Ma, D.; Qiao, W.; Wang, Z. Y. Low -Bandgap Polymers for High Performance Photodiodes with Maximal EQE near 1200 Nm and Broad Spectral Response from 300 to 1700 Nm. *Adv. Opt Mater.* **2018**, *6* (May), No. 1800038.
- (11) Huang, J.; Lee, J.; Vollbrecht, J.; Brus, V. V.; Dixon, A. L.; Cao, D. X.; Zhu, Z.; Du, Z.; Wang, H.; Cho, K.; Bazan, G. C.; Nguyen, T. Q. A High-Performance Solution-Processed Organic Photodetector for Near-Infrared Sensing. *Adv. Mater.* **2020**, 32 (1), No. 1906027.
- (12) Wu, S. E.; Zeng, L.; Zhai, Y.; Shin, C.; Eedugurala, N.; Azoulay, J. D.; Ng, T. N. Retinomorphic Motion Detector Fabricated with Organic Infrared Semiconductors. *Adv. Sci.* **2023**, *10*, No. 2304688.
- (13) Benduhn, J.; Tvingstedt, K.; Piersimoni, F.; Ullbrich, S.; Fan, Y.; Tropiano, M.; McGarry, K. A.; Zeika, O.; Riede, M. K.; Douglas, C. J.; Barlow, S.; Marder, S. R.; Neher, D.; Spoltore, D.; Vandewal, K. Intrinsic Non-Radiative Voltage Losses in Fullerene-Based Organic Solar Cells. *Nat. Energy* **2017**, *2*, 17053.
- (14) Miao, J.; Zhang, F. Recent Progress on Photomultiplication Type Organic Photodetectors. *Laser Photon Rev.* **2019**, *13* (2), No. 1800204.
- (15) Shin, C.; Li, N.; Seo, B.; Eedugurala, N.; Azoulay, J. D.; Ng, T. N. Heterojunction Bilayers Serving as a Charge Transporting Interlayer Reduce the Dark Current and Enhance Photomultiplication in Organic Shortwave Infrared Photodetectors. *Mater. Horiz* **2022**, 9 (8), 2172–2179.
- (16) Wu, Y.; Fukuda, K.; Yokota, T.; Someya, T. A Highly Responsive Organic Image Sensor Based on a Two-Terminal Organic Photodetector with Photomultiplication. *Adv. Mater.* **2019**, *31* (43), No. 1903687.
- (17) Pierre, A.; Gaikwad, A.; Arias, A. C. Charge-Integrating Organic Heterojunction Phototransistors for Wide-Dynamic-Range Image Sensors. *Nat. Photonics* **2017**, *11* (3), 193–199.
- (18) Rim, Y. S.; Yang, Y. M.; Bae, S.; Chen, H.; Li, C.; Goorsky, M. S.; Yang, Y. Ultrahigh and Broad Spectral Photodetectivity of an Organic Inorganic Hybrid Phototransistor for Flexible Electronics. *Adv. Mater.* **2015**, *27*, 6885–6891.

- (19) Yoo, H.; Lee, I. S.; Jung, S.; Rho, S. M.; Kang, B. H.; Kim, H. J. A Review of Phototransistors Using Metal Oxide Semiconductors: Research Progress and Future Directions. *Adv. Mater.* **2021**, 33 (47), No. 2006091.
- (20) Chung, J.; Park, K.; Kim, G. I.; An, J.; Bin; Jung, S.; Choi, D. H.; Kim, H. J. Visible Light-Driven Indium-Gallium-Zinc-Oxide Optoelectronic Synaptic Transistor with Defect Engineering for Neuromorphic Computing System and Artificial Intelligence. *Appl. Surf. Sci.* 2023, 610, No. 155532.
- (21) Iqbal, M. A.; Liaqat, A.; Hussain, S.; Wang, X.; Tahir, M.; Urooj, Z.; Xie, L. Ultralow-Transition-Energy Organic Complex on Graphene for High-Performance Shortwave Infrared Photodetection. *Adv. Mater.* **2020**, 32 (37), No. 2002628.
- (22) Kim, H.; Wu, Z.; Eedugurala, N.; Azoulay, J. D.; Ng, T. N. Solution-Processed Phototransistors Combining Organic Absorber and Charge Transporting Oxide for Visible to Infrared Light Detection. ACS Appl. Mater. Interfaces 2019, 11 (40), 36880–36885. (23) Jeon, S.; Ahn, S. E.; Song, I.; Kim, C. J.; Chung, U. I.; Lee, E.; Yoo, I.; Nathan, A.; Lee, S.; Ghaffarzadeh, K.; Robertson, J.; Robertson, J.; Kim, K. Gated Three-Terminal Device Architecture to Eliminate Persistent Photoconductivity in Oxide Semiconductor Photosensor Arrays. Nat. Mater. 2012, 11 (4), 301–305.
- (24) Ng, T. N.; Chabinyc, M. L.; Street, R. A.; Salleo, A. Bias Stress Effects in Organic Thin Film Transistors. *IEEE International Reliability Physics Symposium*, Phoenix, 2007; pp 243–247.
- (25) Hoshino, K.; Hong, D.; Chiang, H. Q.; Wager, J. F. Constant-Voltage-Bias Stress Testing of a-IGZO Thin-Film Transistors. *IEEE Trans. Electron Devices* **2009**, 56 (7), 1365–1370.
- (26) Street, R. A.; Ng, T. N.; Lujan, R. A.; Son, I.; Smith, M.; Kim, S.; Lee, T.; Moon, Y.; Cho, S. Sol-Gel Solution-Deposited InGaZnO Thin Film Transistors. *ACS Appl. Mater. Interfaces* **2014**, *6* (6), 4428–4437.
- (27) Lee, J. M.; Cho, I. T.; Lee, J. H.; Kwon, H. I. Bias-Stress-Induced Stretched-Exponential Time Dependence of Threshold Voltage Shift in InGaZnO Thin Film Transistors. *Appl. Phys. Lett.* **2008**, 93 (9), No. 093594.
- (28) Ng, T. N.; Russo, B.; Arias, A. C. Degradation Mechanisms of Organic Ferroelectric Field-Effect Transistors Used as Nonvolatile Memory. *J. Appl. Phys.* **2009**, *106* (9), No. 094504.
- (29) Wu, Z.; Li, N.; Eedugurala, N.; Azoulay, J. D.; Leem, D.-S.; Ng, T. N. Noise and Detectivity Limits in Organic Shortwave Infrared Photodiodes with Low Disorder. *npj Flexible Electron.* **2020**, *4* (1), 6.
- (30) Wang, K.; Huang, L.; Eedugurala, N.; Zhang, S.; Sabuj, M. A.; Rai, N.; Gu, X.; Azoulay, J. D.; Ng, T. N. Wide Potential Window Supercapacitors Using Open-Shell Donor—Acceptor Conjugated Polymers with Stable N-Doped States. *Adv. Energy Mater.* **2019**, *9*, No. 1902806.
- (31) Vella, J. H.; Huang, L.; Eedugurala, N.; Mayer, K.; Ng, T. N.; Azoulay, J. Broadband Infrared Photodetection Using a Narrow Bandgap Conjugated Polymer. *Sci. Adv.* **2021**, *7*, No. abg2418.
- (32) Fang, Y.; Armin, A.; Meredith, P.; Huang, J. Accurate Characterization of Next-Generation Thin-Film Photodetectors. *Nat. Photonics* **2019**, *13* (1), 1–4.
- (33) Simone, G.; Dyson, M. J.; Meskers, S. C. J. J.; Janssen, R. A. J. J.; Gelinck, G. H. Organic Photodetectors and Their Application in Large Area and Flexible Image Sensors: The Role of Dark Current. *Adv. Funct. Mater.* **2020**, *30*, No. 1904205.
- (34) Kublitski, J.; Hofacker, A.; Boroujeni, B. K.; Benduhn, J.; Nikolis, V. C.; Kaiser, C.; Spoltore, D.; Kleemann, H.; Fischer, A.; Ellinger, F.; Vandewal, K.; Leo, K. Reverse Dark Current in Organic Photodetectors and the Major Role of Traps as Source of Noise. *Nat. Commun.* 2021, 12 (1), No. 551.
- (35) Ng, T. N.; Wong, W. S.; Lujan, R. A.; Street, R. A. Characterization of Charge Collection in Photodiodes under Mechanical Strain: Comparison between Organic Bulk Heterojunction and Amorphous Silicon. *Adv. Mater.* **2009**, *21* (18), 1855–1859.

- (36) Furchi, M. M.; Polyushkin, D. K.; Pospischil, A.; Mueller, T. Mechanisms of Photoconductivity in Atomically Thin MoS2. *Nano Lett.* **2014**, *14* (11), 6165–6170.
- (37) Yao, W.; Wu, Z.; Huang, E.; Huang, L.; London, A. E.; Liu, Z.; Azoulay, J. D.; Ng, T. N. Organic Bulk Heterojunction Infrared Photodiodes for Imaging Out to 1300 Nm. ACS Appl. Electron Mater. **2019**, *1*, 660–666.
- (38) Sulas, D. B.; London, A. E.; Huang, L.; Xu, L.; Wu, Z.; Ng, T. N.; Wong, B. M.; Schlenker, C. W.; Azoulay, J. D.; Sfeir, M. Y. Preferential Charge Generation at Aggregate Sites in Narrow Band Gap Infrared Photoresponsive Polymer Semiconductors. *Adv. Opt Mater.* **2018**, *6*, No. 1701138.